Pattern characterization of deep-ultraviolet photoresists by near-field infrared microscopy

Bogdan Dragnea, Jan Preusser, Jodi M. Szarko, and Stephen R. Leone[a)]
Departments of Chemistry and Physics, JILA, National Institute of Standards and Technology and University of Colorado, Boulder, Colorado 80309-0440

William D. Hinsberg
IBM Almaden Research Center, 650 Harry Road, San Jose, California 95120-6099

Chemical contrast at subwavelength spatial resolution ($\lambda/10$) is achieved using a fiber-based, infrared near-field microscope, at 3 μm wavelength. Chemically amplified polymer photoresists (poly(t-butylmethacrylate)), patterned by ultraviolet radiation and 250 nm thick, are imaged using infrared (IR) wavelengths situated around the OH stretch band of the polymer, a region sensitive to photochemical changes associated with latent image formation. The key technical points that enable near-field infrared absorption measurements down to 0.05% absorption sensitivity are discussed together with the major contrast mechanisms involved in image formation. The measurements are complemented by confirming studies using confocal infrared microscopy and depth profiling. The exposure dose dependence of the acid catalyzed chemistry, after the postexposure bake step, was studied on line/space patterned samples. The OH subgroup absorption maps of the patterned polymer film exhibit features that are not present in the topographical changes (shrinkage) induced by the postexposure polymer chemistry and illustrate significant potential of the IR near-field microscopy as an analytical tool for polymer chemical physics. *© 2001 American Vacuum Society.* [DOI: 10.1116/1.1340662]

I. INFRARED MICROSPECTROSCOPY

A. Classical infrared microspectroscopy

Microscopic mapping of sample chemistry is essential in very different fields ranging from art restoration to materials science. In many cases, detecting and quantifying chemical modifications of microscopic regions of a sample directly, without special preparation or destruction of the sample, is of utmost importance. Infrared (IR) microspectroscopy is an exceptional tool from this point of view since it relies on the combination of IR spectroscopy and optical microscopy and gives spatially resolved access to the vibrational spectrum of molecules, which is sensitive to the molecular chemistry of the sample. Due to its noninvasiveness, Fourier transform IR microspectroscopy (micro FTIR) is probably the most popular method for chemical microscopy.[1,2] The region of the infrared spectrum which is of greatest interest is the wavelength range 2.5–20 μm (4000–500 cm^{-1}), although the near infrared also has recent applications.[3] The region beyond 5 μm (2000 cm^{-1}) can become quite complex and is often referred to as the ''fingerprint region.'' The chemical structure of composite polymer films can be characterized in this way by a straightforward, model-independent analysis.[4] However, the spatial resolution of FTIR microscopy is limited by diffraction to 2–15 μm, depending on wavelength.

B. Near-field infrared microscopy

The fundamental diffraction limit of classical microscopes is circumvented in near-field scanning optical microscopy (NSOM).[5,6] In this case, the resolution is roughly set by the NSOM probe size, and it depends on the detailed optical interaction between the probe and the sample. The contrast mechanisms of classical IR microscopy are preserved in IR NSOM, whence the appeal of the technique. However, new contrast mechanisms specific to the near field can occur, and care must be taken in the experimental design to obtain results that permit a model-independent analysis.

Although in principle promising, the implementation of infrared near-field microscopy is confronted with several practical problems. One of the aims of this article is to expose these problems and describe several solutions implemented. The solutions are not unique, but are well matched to polymer photoresist characterization. A variety of results demonstrate the ability to probe polymer photoresist materials with chemical subgroup specificity after ultraviolet (UV) exposure and postexposure bake. Beyond these particular material investigations, we believe that careful design of the setup may enable the IR NSOM technique to solve many analytical thin polymer film and biomaterials characterization problems.

II. POLYMER FILM SAMPLES

A. Chemically amplified resists

Features well below 100 nm are now attainable by deep-ultraviolet interferometric lithography[7–9] while electron-beam, extreme UV, and X-ray proximity lithography repre-
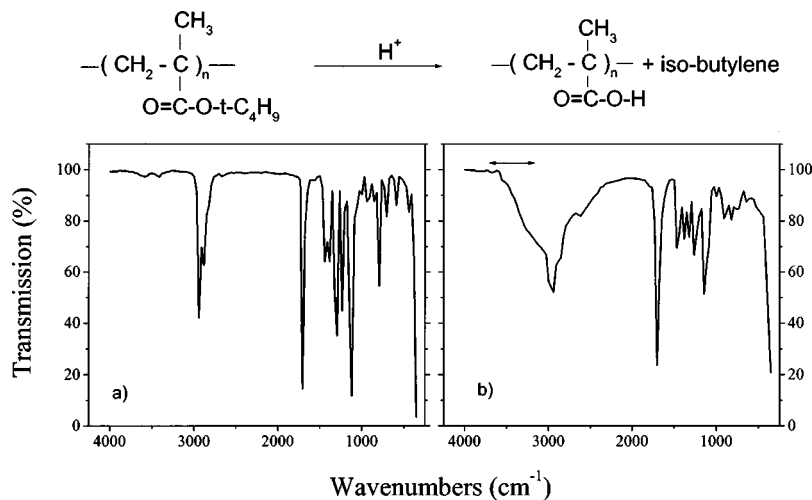
FIG. 1. Infrared spectra of as-coated (left), and irradiated and postbaked films (right). The film before exposure is 3.9 μm thick, while after exposure and postbake some shrinking occurs. The double arrow of the right panel represents the approximate tuning range of the IR color-center laser.

sent future technologies for even higher resolution. All these technologies require high-sensitivity chemically amplified polymeric resists. In this case, the lithographic image formation is the result of three generic steps: exposure, postexposure baking, and dissolution.[10] With exposure, a latent chemically encoded image is formed. The postexposure bake intensifies this image, often by acid catalyzed chemistry. The final dissolution develops the pattern by selectively removing the exposed (positive) or unexposed (negative) resist.

Due to the presence of reactant concentration gradients caused by light intensity variations at the edges, the local chemistry of a submicron feature can be quite different from the bulk. Important phenomena that limit the lithographic resolution are the diffusion of photogenerated acid during the postexposure baking step and random fluctuations in the width of a resist feature, termed line-edge roughness. The line-edge roughness develops at the dissolution step, but it is actually related to the projected (aerial) UV image contrast.[8] The patterned result after the dissolution step, being the last in the process flow, is readily characterized by scanning electron microscopy (SEM) or, for low aspect ratios, by atomic force microscopy (AFM). The postexposure baking step can also be partly characterized by AFM, revealing the topographic changes that generally occur at this stage and even after the exposure step for both negative and positive-tone resists.[11] However, the important chemical changes occurring in these steps may not always simply correlate with the topographic changes. Chemically specific techniques like on-wafer fluorescence microscopy were developed and used to monitor photoacid production.[12,13] However, the fluorescent molecular probes incorporated into the polymer film may affect the acid activity. IR NSOM has certain advantages over the above mentioned methods: it is nonintrusive, it achieves much higher spatial resolutions than conventional optical microscopies, and it generates chemical and topographic images at the same time, offering the ability to follow the chemical modifications directly.

B. Infrared spectroscopy of the resist sample

In transmission NSOM, the transfer of light between the far and the near field occurs with great losses, regardless of the type of microscope in use. Broad spectral sources like those used in micro-FTIR have insufficient brightness for use in near-field microscopy. Therefore, synchrotron radiation or IR lasers are required for near-field spectroscopy.

We use a cw color-center laser (2–4 mW), pumped by a Kr^+ ion laser, tunable from 2.3 to 3.25 μm (4350–3075 cm^{-1}). In this spectral region, both C–H and O–H stretching vibrations have absorption bands. The C–H stretch is ubiquitous in organic molecules, and the OH bond is advantageous for chemically selective microscopy. We chose therefore to study the poly(tert-butylmethacrylate) (PTBMA) photoresist, one specific example from a family of acrylate photoresists that show promise for deep-UV lithography,[10] and whose deprotected form, poly(methacrylic acid) (PMAA) has an O–H functional group. The resist samples are films of PTBMA containing 5 wt % of the photoacid generator triphenylsulfonium hexafluoroantimonate. To illustrate the spectral changes, the two IR spectra presented in Fig. 1 are recorded at different points in the process. For routine infrared spectra, the PTBMA film was prepared by spin coating a solution of the polymer onto a sodium chloride plate and then heating on a hot plate at 130 °C for 5 min to drive off the casting solvent. The spectrum on the left was recorded with a FTIR after the postapply bake. The film thickness at this point was 3.9 μm. The film was then exposed to UV light in the range of 200–300 nm, which causes the photoacid generator to form hexafluoroantimonic acid. The exposed film was heated at 130 °C for 5 min, which activates the thermal deprotection chemistry. The spectrum on the right was recorded at this point. Evolved gaseous isobutylene (Fig. 1) leads to a somewhat thinner film. The most prominent changes in the IR spectra are the appearance of a broad hydroxyl absorption in the frequency region 2500–3500 cm^{-1} and the loss of several absorptions associated with the *t*-butoxy group in the range

$800-1500 \text{ cm}^{-1}$. The films prepared for IR NSOM studies were 250 and 1000 nm thick, PTBMA plus photoacid generator on sapphire substrates, exposed using a contact mask with a pattern of UV light at 250 nm wavelength and postbaked. The maximum UV dose was 21 mJ/cm^2.

III. IR NSOM APPARATUS

The NSOM apparatus is based on the coated-fiber method developed by Betzig *et al.*[14] and on the tuning-fork approach of Karaï and Grober,[15] for the shear-force feedback control. Infrared transparent fibers composed of zirconium aluminum fluoride, transparent from 0.45 to 5.0 μm, are used.

A. Infrared fiber tips

The inherently inefficient transfer of light energy between the near and far fields is the major problem in near-field microscopy. This problem is exacerbated by the use of IR wavelengths. For aperture microscopes based on optical fibers,[14] maintaining the same size aperture while transmitting longer wavelengths through the fiber requires longer evanescent propagation distances in the evanescent mode through the taper. Therefore, special techniques must be applied to create a low aspect ratio taper. Multiple step processes such as variable-pulling rates,[16] or combinations of selective etching, pulling, and focused ion beam milling,[17,18] all aim to produce a multiple taper structure, which improves the throughput by orders of magnitude with respect to single-taper fibers. In the present work fiber tips obtained by the variable-pulling method were used.[16] The tips were fabricated from fluoride glass fibers, transparent between 0.45 and 5.0 μm. They resemble a steeple-on-a-mesa, with a 200–300 nm aperture obtained by lateral coating with 120 nm thick Al by thermal evaporation in a custom-built vacuum chamber with a base pressure of $\sim 10^{-6}$ Torr (7.5 $\times 10^{-3}$ Pa).[16,19] The deposition rate was 5–10 nm/s. A quartz microbalance was used to monitor the rate of deposition and the thickness of the metal film. The tips were fixed at an angle of 40° and rotated continuously at a rate of $\sim 2 \text{ s}^{-1}$ during the coating process. Since the reproducibility of the tip fabrication critically depends on pulling parameters, the fibers were checked prior to use by two methods. By SEM we measured *ex situ* the aspect ratio, the coating quality, and the aperture size of the tip. The optical quality of the aperture was characterized by sending 633 nm light into the fiber and focusing the light emerging from the aperture through a microscope objective onto a charge coupled device camera. Ideally, the far-field pattern recorded by the camera should match the diffraction pattern for a subwavelength aperture (the Airy diffraction pattern). Occasionally, leakage of the 633 nm light was noticed. In this case the Airy disk pattern is strongly perturbed. We presume that the cause of the leakage is roughness of the Al coating. The metal film coating quality depends on deposition rate, and vacuum, as well as on the initial fiber preparation (stripping of the polymer cladding).

The far-field throughput of our fiber tips at 3 μm wavelength is $10^{-4}-10^{-5}$ relative to the throughput of a cleaved fiber.[16] The percentage of successful pulled tips is roughly $\sim$50%, but we found that it depends on the fiber batch; fibers with the same specified optical characteristics, but from different manufacturers, behaved quite differently during the pulling.

An increased interest arose in the last years to use chalcogenide glass fibers.[20,21] These fibers have a larger IR transparency range, up to 11 μm, but are not transparent in the visible, and they can be conveniently etched, producing tips with good throughput at long wavelengths.[22] However, fiber etching leaves the taper much rougher when compared to pulled fibers. This fact could allow lateral leakage of light through the subsequently deposited metal coating, which makes the fabrication of a circular aperture difficult.

In the case of apertureless microscopes (using AFM tips),[23–26] the near-field scattered intensity varies with the wavelength λ as λ^{-4}, and therefore in this case it is also more difficult to couple light at IR wavelengths. The extraction of the near-field signal from the far-field background scattered by the AFM tip is a difficult but solvable technical problem, requiring special optics for the IR. The apertureless microscope represents a promising method; since it has no spectral limitations, it lacks the lossy evanescent transmission region of the fiber tips, and it can take full advantage of the well-developed AFM technology.

B. Detection

For IR radiation at 3 μm, a good detector is the liquid nitrogen cooled photovoltaic InSb detector. However, this detector is much less sensitive than a photomultiplier working in the visible. Because detectors of this type have detectivities approximately 4 orders of magnitude lower than photomultipliers, great care must be taken in the IR NSOM setup to maximize the detection sensitivity and light collection. A photovoltaic InSb detector is often limited by the shot noise in the amplifier or by the background IR radiation. If the detector is limited by the background IR radiation, the noise current can be decreased in two ways: first, by providing the detector with a cold field of view, and second, by using a small area detector. Our detectors have an active area of 0.015 mm^2 and a cooled field of view of 10°. The calculated detectivity is in this case $\sim 10^{12}$ cm Hz$^{1/2}$/W (at 1 kHz). The electronic bandwidth of the detector is 0.1 Hz–1.5 kHz.

In practice, the largest source of noise is frequently the laser intensity stability. The sensitivity of detection can be improved by rejecting the laser amplitude noise in a differential scheme, Fig. 2. The recorded variables are the same as in a traditional transmission spectrophotometer. The laser beam is chopped at 1 kHz, and lock-in detection of the signal/reference is performed with a bandwidth of $\sim$100 Hz. Due to the bandwidth limit, a scan of 256×256 pixels takes at least 15 min.

Thorough vibration control of the NSOM within the 0.1–500 Hz range is achieved by having a massive body for the NSOM instrument itself and positioning the instrument on a floating benchtop. In a closed loop, (constant shear force) the system is characterized by a vibrational noise of
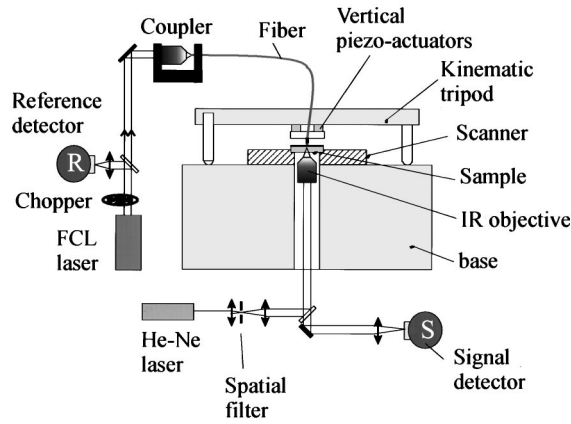
FIG. 2. Schematic of experimental setup. The reference and the sample signals from the pinhole detectors R and S are fed to the differential input of a lock-in amplifier, locked on the chopper frequency (1 kHz). The NA of the IR objective is important for the establishment of the contrast mechanism. The spatially filtered He–Ne laser beam is used as a pilot beam for alignment, as well as for confocal reflection microscopy (the signal detector is replaced in this case with a Si photodiode).

~ 3 Å Hz$^{-1/2}$, a value comparable with the thermal displacement noise of the tip at room temperature.[27] The near-field IR light exponentially decays from the sample surface, and therefore the mechanical noise is greatly amplified in the optical signal arm. This is the reason one has to minimize the system vibrations within the optical detection bandwidth. Less high-frequency mechanical noise also extends the tip lifetime.

IV. INFRARED IMAGE FORMATION

In previous work on the same type of films,[16] it was shown that the IR NSOM contrast between exposed/postbaked and unexposed lines was greater than what one would expect from simple absorption. As the images were taken in both constant gap and constant height modes without important changes in contrast, we ruled out the possibility of topographic artifacts.[28] The high contrast of images in Ref. 16 was explained by the division of the far-field emission pattern into two collection angle regions: an allowed

and a forbidden zone.[28] The sample interfaces are parallel in our setup and some of the light rays emerging from the NSOM aperture were totally reflected by the sapphire substrate at the air interface. The angle of the ''allowed'' light cone depends on whether the tip is positioned above an exposed or unexposed region of polymer, because of a difference in the indices of refraction. When the numerical aperture (NA) of the collection objective is greater than the ''allowed'' light cone, this angular difference generates the main contrast, which is refractive in origin. For analytical purposes we are interested mainly in chemical subgroup specific pure absorption contrast, and one way to separate this contribution from the larger, refractive contribution is to decrease the NA of detection. Having the collection angle smaller than the minimum critical angle will minimize the angular differences between the allowed light cones. The results of the present work are all acquired in this way. There still will be some refractive contributions from reflectivity differences, from the nonisotropic angular distribution within the light cone, and from variations of the refractive index in the vicinity of an absorption band (Kramers–Krönig relations). Some of these effects have been calculated[16] and shown to be negligible. Later we will discuss an experiment to determine if the low NA approximation is legitimate.

A. IR confocal microscopy results

When pure absorption contrast is achieved, the results should not be different between the near and far field. A far-field confocal microscope was used to image a patterned film whose thickness (500 nm) was well below the wavelength of the light (~ 3 μm). In this situation (far field and thin films), the importance of the refractive mechanism is greatly decreased. We obtained images of 8 μm line features written in the polymer photoresist and after the postexposure bake, only in the wavelength range of 2.95–3.02 μm (within the OH band), and no contrast at wavelengths shorter than 2.75 μm (off the band) (Fig. 3). The images in Fig. 3 measure essentially the pure absorption contrast, as expected. Using a multiple reflection model, we calculated the expected contrast for a 250 nm thick film, for an absorption coefficient of $\alpha = 0.042$ μm^{-1} for PMAA, at 3 μm wave-
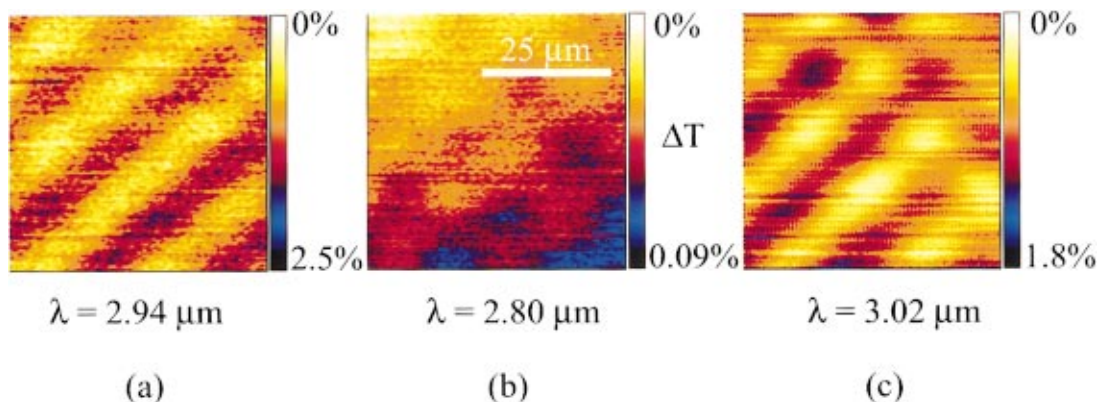

FIG. 3. IR confocal microscopy images, 50×50 μm, of an exposed and postbaked PTBMA/PAG sample, at three different wavelengths: (a) 2.94 μm, (b) 2.80 μm, and (c) 3.02 μm. The film was 250 nm thick on sapphire. Wavelengths that are not within the O–H absorption band do not achieve contrast.

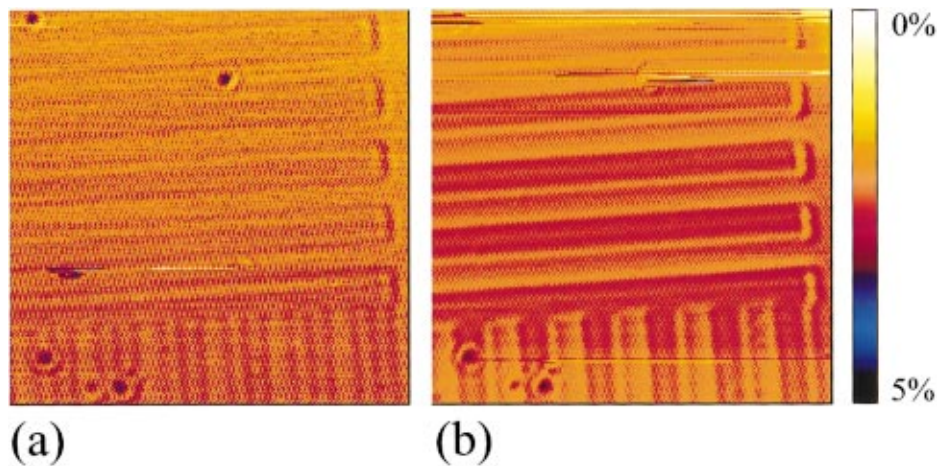FIG. 4. IR NSOM images of a 8 μm/8 μm line/space pattern written by DUV exposure and postexposure bake on a 1 μm thick chemically amplified, photoresist film. The images are taken at: (a) 2.80 μm wavelength and (b) 2.94 μm wavelength in the constant height mode.

length and with a collimated beam. We predict a value of 1.6%. In reality, the beam is divergent through the length of the film, and this value is an underestimate because of the longer path length. In the images of Fig. 3 we obtained an experimental transmission contrast of $2.0\% \pm 0.3\%$, close to the predicted value. The estimated error in the experimental measurement corresponds to the large scale spatial variations observable on infrared images taken at slightly different wavelengths (Fig. 3). We believe these variations reflect a nonuniform illumination field at the fiber end.

The small disagreement between the calculated and the experimental values for the contrast might be also due to the fact that confocal microscopy is sensitive to interface variations, not only to the optical constants.[29] Nevertheless, this should be only a weak effect since the shrinkage of the exposed and postbaked film is ~100 nm for a 21 mJ/cm^2 dose, while the depth of field of the confocal microscope is ~25 μm. The 100 nm change in thickness was measured on blank (unpatterned) films, processed under the same conditions as the patterned samples.

B. IR near-field results

Having obtained encouraging contrast with the confocal setup, the same detection scheme (with reduced NA) was used with a near-field tip. The same pattern (8 μm/8 μm line/space) was imaged in the constant height mode. In this case, the shear-force feedback is disabled. The average tip height above the surface was ~250 nm. The film thickness was 1 μm. Due to the open loop, large area scans are possible at a reasonable speed. As discussed later in this article, images acquired in this mode are also expected to exhibit fewer topographic artifacts.[30] The IR NSOM images from Fig. 4 were taken at two different wavelengths: 2.80 μm (a) and 2.94 μm (b). One can easily notice the spectroscopically enhanced contrast in image (b) as compared to image (a). The image quality shows considerable improvement with respect to the confocal IR microscopy pictures in Fig. 3. The image taken at the 2.80 μm wavelength still shows some contrast, mainly at the borders between the irradiated and nonirradiated areas. Since we expect ~400 nm shrinkage of the 1 μm thick film upon postexposure bake, the deep edge

formation could explain the presence of contrast via refractive mechanisms. For this reason, for the rest of this article, we will discuss only data that were acquired on thinner films (250 nm thick). One should also note that the vertical edges of the features in Fig. 4 are sharper than the horizontal edges. This is more apparent in image (a). Since the IR radiation is linearly polarized, it is possible that the enhancement of the edge contrast is a polarization effect. A similar effect has been described in the literature.[31] However, the previous work was done in reflection, at constant gap, and on metal structures. Because of all these differences, it is difficult to conclude whether the polarization effect has the same origins or not.

To obtain maximum spatial resolution, the near-field images need to be acquired in the constant gap mode (~10 nm, using shear-force feedback). Constant shear-force (topographic) and IR images at 2.97 μm wavelength, for a 1 μm/1 μm line/space pattern on a 250 nm thick film are presented in Fig. 5. Average horizontal cross sections of the IR and topographic images are also included. This line/space pattern is close to the limits of this particular NSOM tip in terms of spatial resolution. Thus both the contrast and clarity of the image are degraded compared to images of wider spaced lines. The deeper zones in the topographic image correspond to more strongly absorbing zones in the IR image, as expected. The UV dose was 21 mJ/cm^2. The maximum absorption modulation, 0.5%, is less than the expected value from the experimental determinations in far field. Here we define the absorption modulation as the difference between the peak and the valley signals divided by the average signal. Below 2.8 μm wavelength there was no contrast at all in the optical scans. It is important to emphasize here that in Ref. 16, where a high NA collection was used, we observed ~10% optical contrast even at nonresonant wavelengths. The results suggest that the present near-field data are close, indeed, to a pure absorption contrast.

The shrinkage of the polymer in the topographic image of Fig. 5 has four weak local maxima (~3 nm high) along the unexposed lines (light regions). This secondary pattern in the region of the geometrical shadow of the mask may be explained by diffraction of the UV light (250 nm wavelength)

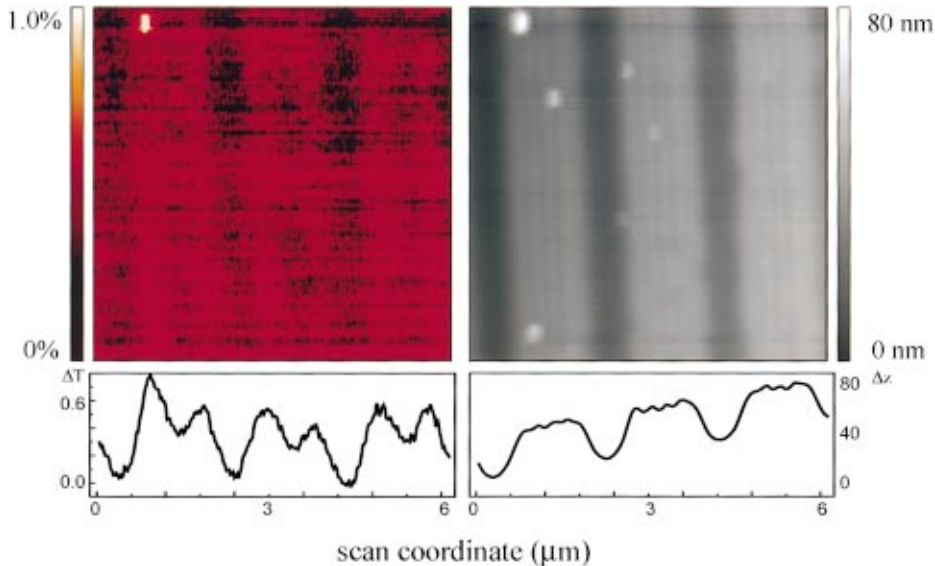FIG. 5. IR NSOM optical and topographic (constant shear force) images of 1 μm/1 μm line/space pattern on 250 nm thick film: exposure dose: 21 mJ/cm^2, scan range: 6.25 $\times$ 6.25 μm, and IR wavelength: 2.97 μm. The cross sections were averaged over 100 scan lines.

on the proximity mask edges and interference of the secondary waves within the geometrical shadow region.[19] In the IR image, the unexposed lines have a comparatively deeper single secondary maximum (Fig. 5). It is interesting to note that merely having a lower optical resolution than the topographic resolution cannot explain why the secondary minimum in the absorption image is so deep. Making a convolution of the secondary topographic structure with a large optical aperture would only wash out the structure. The difference suggests that the polymer shrinking does not follow the same dependence on the photochemistry and postexposure bake chemistry, at least at the low exposure levels involving the unexposed areas.

A simple scalar Kirchoff–Fresnel approach for near-field diffraction on amplitude masks also indicates the presence of a significant level of UV exposure within the masked regions.[19] Since the maximum dose of 21 mJ/cm^2 is close to saturation, a residual UV level in the unexposed regions will decrease the contrast of the latent image with respect to the one expected from a geometrical shadow approach. On larger line/space patterns, as those from Fig. 3, the edge effects at the UV exposure step are not important and therefore the contrast is closer to the value expected from the geometrical shadow model.

1. IR sensitivity and optical resolution

The apparent spatial resolution of the IR image from Fig. 5 is at least 500 nm. The nonaveraged signal-to-noise (S/N) ratio is ~2. In addition to the pattern smearing due to interference, we found that another cause for the small S/N value is the angular pointing stability noise of the Kr$^+$ laser beam that pumps the color-center laser, thus affecting the pointing of the color-center beam. The I versus I_0 detection does not work in this case since the reference and the signal beams have different responses to angular perturbations. Since this is a very low frequency noise, it can be seen in the optical image of Fig. 5 as horizontal streaks. However, the averaged line scan (over 100 lines) has a better S/N ratio (~20).

Therefore, in the averaged mode, much thinner films (down to 50 nm thick) could be characterized, at this resolution, with an absorption sensitivity of ~0.05% (cf. Fig. 5, line scan graph).

Due to the fact that the fiber tip throughput decreases rapidly with decreasing aperture diameter, a tradeoff exists between spatial resolution and absorption sensitivity. If we consider the same film thickness of 250 nm, smaller apertures down to 150 nm could be employed. To calculate the minimum aperture diameter of 150 nm, which gives a S/N ratio of 1 *in the averaged mode*, we started with a S/N ratio of 100 for a 300 nm aperture and supposed that the optical throughput scales as the fourth power of the aperture radius.[32] For lateral characterization at resolutions beyond 150 nm, other methods will need to be employed. In particular, the problem of acid diffusion, during postexposure bake, will require a better spatial resolution. The positive-tone chemically amplified resists based on acrylic polymers are used in advanced deep ultraviolet (DUV) photolithography applications, where the resolution requirements generally exceed the 150 nm limit expected for the present aperture-mode NSOM instrument. However, the photoacid diffusion problem can be still treated given that the acid mobility varies strongly with the temperature. Characteristic lengths greater than the optical resolution can then be obtained, by adjusting the postexposure bake time and temperature. To what extent the results may be extrapolated to smaller length scales remains to be established in the future.

The observed ratio between the full width at half maximum (FWHM) of the exposed and unexposed lines in Fig. 5 is not unity as might be expected from the binary mask pattern. This fact, too, could be explained at least partly by the interference pattern occurring behind the mask during the UV exposure. In the case of the topographic features that correspond to the exposed zones, the apparent lateral narrowing possibly contains some contributions from the low aspect ratio NSOM tip. Deep features in topography cannot be reached by the tip, and the resulting topographic image is a
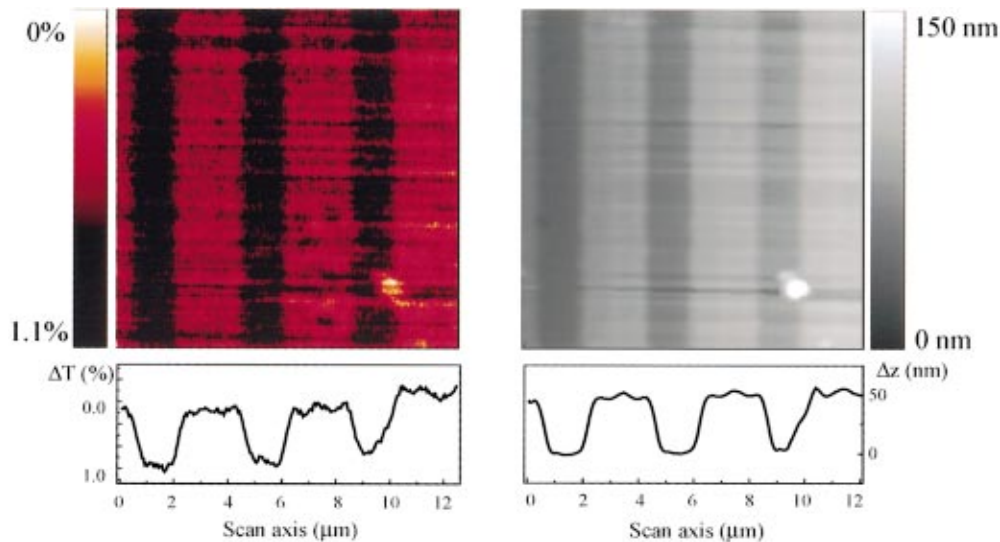
FIG. 6. IR NSOM optical and topographic (constant shear force) images of 2 μm/2 μm line/space pattern on 250 nm thick film: exposure dose: 21 mJ/cm^2, scan range: 12.5×12.5 μm, and IR wavelength: 2.97 μm. The optical spatial resolution was evaluated from the modulation transfer function to 300 nm. The cross sections were averaged over 100 scan lines. The sample tilt was subtracted from the topographic cross section.

spatial convolution between the tip shape and the real feature. The tip shape effect can be expressed as a depth-dependent lateral resolution of the shear-force technique: large height variations can be probed only when they occur on a long-range lateral scale. In the case of the optical image, the IR beam emerging from the aperture can be considered collimated over distances comparable to the aperture diameter.[33] This means that the entire thickness of the polymer film (250 nm) is probed by the light with the same lateral spatial resolution, and the FWHM of the IR line is likely to be a true representation of the linewidth. We theoretically estimated the minimum UV exposure within the shadowed areas.[19] The diffracted UV light also results in the narrow series of ridges observable on the top of unexposed lines in the topographic image. For a 2 μm/2 μm line/space pattern the diffracted UV exposure is ~2.5% of the peak exposure, while for the 1 μm/1 μm line/space pattern the diffracted UV exposure reaches ~5.2% of the peak value. Because of acid catalyzed chemical amplification during the postexposure bake, the residual UV light from the unexposed areas leads to a decrease in contrast of the latent image. As a consequence, the relatively low contrast of the nonaveraged 1 μm pattern made us try larger features, 2 μm line/space, for which the smearing of the aerial UV pattern due to interference contributions should be less. Another consequence of the residual (diffracted) UV exposure is an increase in IR absorption in the center of the unexposed lines, as a result of the deprotection chemistry. This creates an appearance of line doubling, a phenomenon that has been encountered in studies of metal diffraction gratings by reflection NSOM.[34] The two experiments differ, however, because: (1) the ''double beating'' as well as most of the contrast disappears in our experiment when working at nonresonant wavelengths; (2) the IR patterns presented here have a correspondence in topography, although the IR and topographic maps are qualitatively different; and (3) the data in Ref. 34 concern

reflection-mode near-field microscopy and metal gratings, as compared to transmission microscopy and dielectric gratings in the present work.

The results of Fig. 6, taken with 2 μm/2 μm line/space features, show higher contrast at 10.3 mJ/cm^2 UV dose, than the 1 μm pattern in Fig. 4 at 21 mJ/cm^2. The optical image of the film appears to be more inhomogeneous in the bottom-right corner of the IR image, while the topographic image does not show the same perturbations, except for the raised bright spot, which is probably a dielectric particle. The domains in the IR image that do not correspond to noise streaks in the topographic image were observed in many of the IR images. They have a lateral size of ~500 nm and represent differences in IR absorption of 0.1% with respect to the nonexposed surface. Their origin is not known at the moment, but their existence illustrates very well the potential of the method.

The higher contrast on this pattern allows us a better consideration of the question of spatial resolution. There is a periodic signal on one axis and by examining the Fourier transform of the signal it is possible to establish the modulation transfer function of the microscope.[35] In Fig. 7 we compare the amplitudes of the Fourier transforms of the IR and topographic line scans, as well as the calculated incident UV intensity. In Fig. 7 we used the set of data from Fig. 6. One can see that the optically transmitted spatial frequency peaks span at least up to 320 nm (3.13 μm^{-1}), which represents the same resolution limit as in Ref. 16.

2. Comparison between the infrared and scanning force characterization: Exposure dose dependency

The Fourier transforms of the topographic and IR signals are qualitatively similar (Fig. 7). This is not surprising considering that the shrinkage should be proportional to the
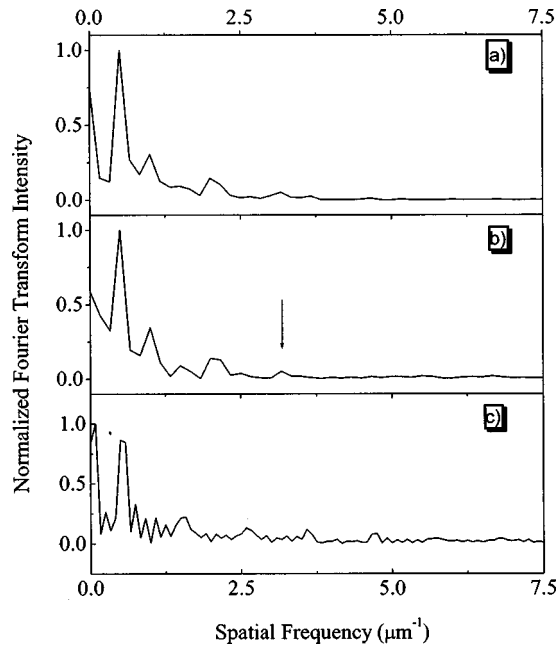
FIG. 7. Fourier transform spectra of: (a) topographic and (b) infrared line scans from Fig. 6. For comparison, the calculated near-field UV intensity distribution was added (c). The calculations took into account the Fresnel diffraction at the mask edges. The arrow indicates the highest transmitted spatial frequency, corresponding to ~320 nm resolution.

deprotection reaction. However, modifications to the specific volume of a polymer (as shrinking) are the result of complex phenomena,[36] while the IR absorption modulation is, in principle, determined by a much simpler relationship to the acid catalyzed chemistry. The IR images are directly related to the number of OH subgroups and their absorption strength. The connection between the shrinkage and the IR spectra can provide valuable information on the physico-chemical processes occurring during the exposure and postexposure bake steps. To quantify the IR/shrinkage connection we studied how the IR and the topographic lines change with the expo-

sure dose. The cross-sectional area of an exposed line, measured by IR NSOM, should be proportional to the poly-methacrylic acid concentration — the deprotected form of poly(tert-butyl methacrylate). Figure 8(a) shows the normalized variations of both topographic and IR line-scan *integrals* of exposed lines with UV dose. The data were collected by imaging patterns of 2 μm/2 μm line/spaces obtained at different exposure levels between 10.3 and 21 mJ/cm^2, at the same postexposure bake conditions. While the topography varies only within 18% of the maximum exposure case, the IR modulation has 55% variations.

The measured topographic FWHM of exposed lines was remarkably constant ($1.61 \pm 0.02 \mu$m) throughout the entire set of different exposures, whereas the modulation peak integral varies. This fact indicates that the topographic modulation is not limited by the width of the tip. For a tip-limited measure, there could not be depth modulation changes without width variation. Therefore, the tip reaches at least partly to the bottom of the exposed lines. The IR (exposed) lines are $1.62 \pm 0.04 \mu$m in good agreement with the topographic measures.

In Fig. 8(b) we plotted the modulation of the IR signal against the amplitude of shrinkage modulation. We used the data from Fig. 8(a), and also, in order to extend the survey to small dose values, we used the 1 μm/1 μm line/space main modulation in Fig. 5, as well as the small modulation interference on the top of unexposed regions (3 nm on the topographic images) due to the UV leakage under the mask. We consider it important to note in Fig. 8(b) that for the small exposures the IR signal is stronger, relative to the shrinkage. Although the shrinkage (topographic) measurements and IR measurements show results similar to the dose, the nonlinear dependency in Fig. 8(b) indicates that a threshold UV dose is necessary before the shrinkage may occur. Using the same formalism as in Ref. 19, and extrapolating the experimental data from Fig. 8(b) one can estimate an upper limit of the shrinkage threshold dose at ~1 mJ/cm^2. To explain the
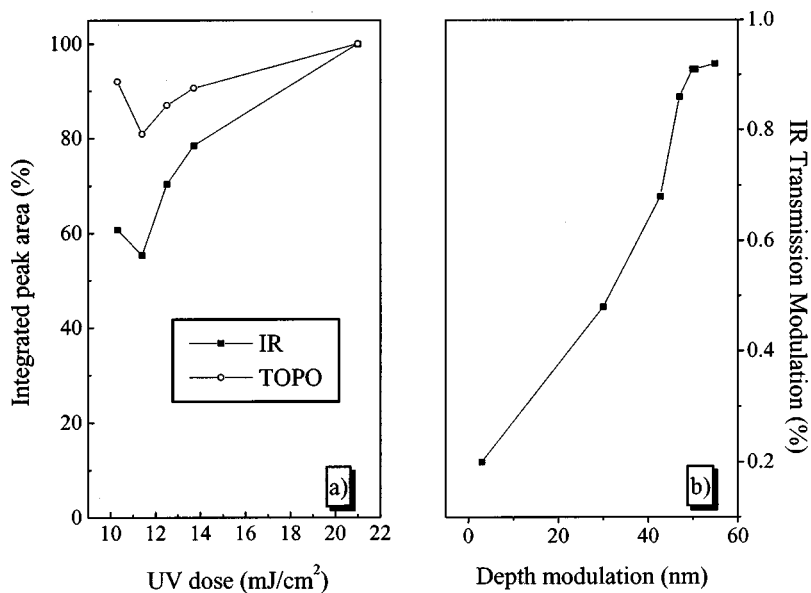

FIG. 8. (a) Depth and absorption modulation peak integrals as measured by IR NSOM on 2 μm/2 μm line/space patterns, at various UV exposures. (b) The correlation between the absorption modulation and the depth modulation. The smallest modulations on the graph come from data at 1 μm line/space. The smallest exposure was ~1.2 mJ/cm^2.
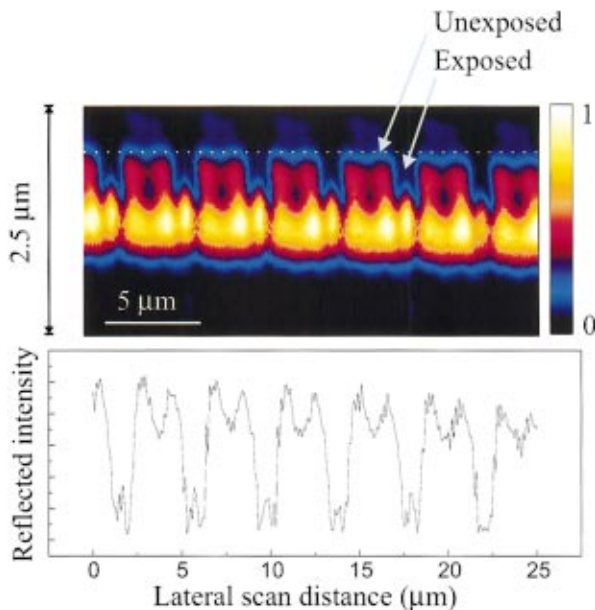
FIG. 9. Confocal depth scans and cross-section plot across a 2 μm/2 μm line/space pattern: vertical scan range: 2.5 μm, horizontal scan range: 25 μm, exposure: 42 mJ/cm^2, and film thickness before processing: 1000 nm. The horizontal line locates the cross section on the density plot.

threshold (and nonlinear relation between the IR and topographic modulation) we propose that, at small doses, the volatile reaction product (isobutylene) remains trapped in the polymer matrix and the associated polymer swelling balances the shrinkage.

We verified that the line–space width differences indeed occur by using the optical sectioning property of confocal microscopy. We used 633 nm light with a reflection confocal setup sketched in Fig. 2. The lateral resolution was estimated experimentally at $\sim$360 nm, while the depth of focus was 680 nm. When in focus, the 2 μm line patterns present planar interfaces to the incident beam, and the theory behind the depth profiling under these conditions is well developed.[29] Instead of scanning the sample in the horizontal xy plane to get an image, we scan perpendicular to the pattern lines x while scanning in the z direction, normal to the surface. The resulting pattern is known as a ''cloud'' plot and has been used in the past for resist characterization.[35] The image in Fig. 9 gives such a plot taken on a 1000 nm thick film, with a 2 μm/2 μm line/space pattern. The expected shrinkage from nonpatterned samples is 39% or 390 nm. The variation in the indices of refraction from PTBMA to PMAA is small ($\Delta n = 0.05$). Because of this small difference, the image contrast in Fig. 9 is generated mainly by the topography at the different interfaces convoluted with a function that describes the light intensity distribution in the focal zone of the microscope objective.[29]

In Fig. 9 the exposed lines are narrower than the unexposed ones. The FWHM of exposed lines is 1.51 μm, in good agreement with the near-field measurements. We calculate from data in Fig. 9 the relative positions of the polymer surfaces. In order to do this we first find the depth response of a perfect mirror and then deconvolute it from the

density plot of Fig. 9. The height difference between the exposed and unexposed interfaces is 300 nm, or 30% shrinkage. This agrees with the data obtained by IR NSOM, but disagrees with the measurements obtained on unpatterned samples. Both features, unequal line/spacing and smaller than expected shrinkage, are most likely due to interference of the scattered UV beam on the mask edges. This interference will distort the patterned image and decrease the contrast, and therefore the shrinkage, by irradiating both shadowed and exposed zones at the same time. It is worth noting that when the line dimensions are considerably larger, and the edge effects are relatively small, as is the case in Figs. 3 and 4, exposed and unexposed zones are equally spaced.

3. Far-field contributions

The question arises whether in a transmission microscope, like the one used in this work, the far-field contributions will interfere with the near-field measurements. It is known that the spatial resolution remains approximately constant at depths comparable with the aperture diameter.[33] This limits the applicability of the IR NSOM to a superficial depth of $\sim$300 nm.

For films that are thicker than 300 nm, some far-field contributions exist in the IR NSOM images.[16] However, due to the angular spread of the light, these contributions are efficiently averaged in the far field and in many cases will be negligible. For example, for a linear scan of 10 μm, and considering an emitting dipole-type angular distribution at 100 μm from the surface, the diameter of the irradiated area is $\sim$400 μm. The maximum modulation of the total signal, from one side of the scan to another and due to features present in this plane, is only $1/40^2$ ($\sim$0.6%).

4. IR NSOM spectroscopy

The relatively small tuning range of the available IR laser does not yet allow for detailed spectroscopic studies. Tuning the wavelength on and off the OH absorption band will alter the image contrast, as expected from far-field measurements. The average behavior of the IR NSOM contrast at two different regions of the spectrum is depicted in Fig. 10, where 2 μm/2 μm line/space features were imaged in the constant gap mode (shear-force feedback control). The chemical-subgroup-specific probing is demonstrated by the contrast changes in the IR NSOM images. Nevertheless, we found that tuning the wavelength in small steps (5 nm) between 2.75 and 3.1 μm brought about unexpectedly strong spectral variations. We found that these spectral perturbations are not related to the sample, but to the fluoride fiber. We tested a cleaved fiber at both ends (without a tip) and found that in very narrow spectral windows (5–10 nm) the fiber transmission shows changes up to 50%. The density and magnitude of the above spectral perturbations are proportional to the length of the fiber, and we suppose that they are caused by the presence of scattering/absorption centers which perturb the modal distribution, and therefore the transmission as a
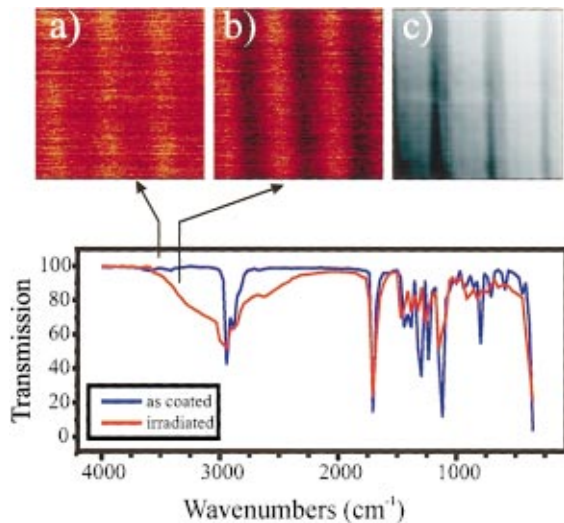
FIG. 10. IR absorption in the UV exposed lines results in contrast variations of optical images (12.5×12.5 μm) taken at two different wavelengths: (a) 2.85 μm and (b) 2.94 μm. In (c) topographic image (dark, exposed lines are deeper).

function of wavelength. We found a critical fiber length for this effect of ~200 mm. Below the critical fiber length the spectral perturbations could be neglected.

C. Topographic artifacts

It is known that samples with large surface morphology can induce topographic artifacts in optical images taken in the constant gap mode (with shear-force feedback, for example).[28,37] The fact that we obtain wavelength-dependent contrast extinction, as shown in Fig. 10, indicates that the topographic artifacts are limited and not deleterious. In addition, similar contrast is obtained in constant height images and in constant gap mode images. Also, the near-field contrast ratio is in agreement with the far-field contrast, and the values match well those expected from simple absorption. The complex correlation between the topography and the absorption modulation from Fig. 8 is not indicative of the prevalence of topographic effects over optical effects, because both topography and absorption have a common origin: the acid catalyzed chemistry that occurs at the post-exposure bake step. Moreover, in Fig. 8 one can see that by extrapolation of the existing data a certain amount of absorption may exist even when the shrinkage is zero. When topography is present, the long wavelength and the relatively large NSOM apertures used ensure that the topographic artifacts do not display a measurable contribution.

V. CONCLUSIONS

In conclusion, near-field infrared microscopy was applied to chemically amplified resist characterization after the post-exposure baking step. Using a small NA for light collection, the absorption contrast was decoupled from the refractive contrast. The infrared near-field transmission microscope uses fibers with a multiple taper structure and optimized throughput. On resist samples, the present resolution is lim-

ited by the differential detection sensitivity (0.05%) to 320 nm (λ/10). The IR images of polymeric resists show correlations, but also differences between the topography induced by the acid catalyzed chemistry and the characteristic IR absorption of the deprotected polymer. The differences can be noticed mainly in the region of low UV exposure doses, where negligible shrinking of the exposed zones occurs, but IR contrast persists. By correlating the IR NSOM experiments with confocal metrology it was found that the deprotection yield is different for narrow line/space patterned samples than for blank samples. The main reason is edge interference effects occurring in the UV exposure step when binary proximity masks are used.

[1]D. L. Wetzel and S. M. LeVine, in *Infrared and Raman Spectroscopy of Biological Specimens*, edited by H.-U. Gremlich and B. Yan (Dekker, New York, 2000).
[2]P. M. Cooke, Anal. Chem. **70**, 385R (1998).
[3]W. F. McClure, Anal. Chem. **66**, 43A (1994).
[4]J. L. Koenig, *Microspectroscopic Imaging of Polymers* (American Chemical Society, Washington, DC, 1998).
[5]D. W. Pohl, W. Denk, and M. Lanz, Appl. Phys. Lett. **44**, 651 (1984).
[6]R. C. Dunn, Chem. Rev. **99**, 2891 (1999).
[7]T. A. Savas, M. L. Schattenburg, J. M. Carter, and H. I. Smith, J. Vac. Sci. Technol. B **14**, 4167 (1996).
[8]W. D. Hinsberg, F. A. Houle, J. Hoffnagle, M. Sanchez, G. Wallraff, M. Morrison, and S. Franck, J. Vac. Sci. Technol. B **16**, 3689 (1998).
[9]H. H. Solak, D. He, W. Li, and F. Cerrina, J. Vac. Sci. Technol. B **17**, 3052 (1999).
[10]W. D. Hinsberg, G. M. Wallraff, and R. D. Allen, *Kirk-Othmer Encyclopedia of Chemical Technology*, 4th ed. (Wiley, New York, 1998), p. 233.
[11]L. E. Ocola, F. Cerrina, and T. May, J. Vac. Sci. Technol. B **15**, 2545 (1997).
[12]P. M. Dentinger, B. Lu, J. W. Taylor, S. J. Bukofsky, G. D. Feke, D. Hessman, and R. D. Grober, J. Vac. Sci. Technol. B **14**, 4239 (1996).
[13]B. Lu, J. W. Taylor, F. Cerrina, C. P. Soo, and A. J. Bourdillon, J. Vac. Sci. Technol. B **17**, 3345 (1999).
[14]E. Betzig, P. L. Finn, and J. S. Weiner, Appl. Phys. Lett. **60**, 2484 (1992).
[15]K. Karraï and R. Grober, Appl. Phys. Lett. **66**, 1842 (1995).
[16]B. Dragnea, J. Preusser, W. Schade, S. R. Leone, and W. D. Hinsberg, J. Appl. Phys. **86**, 2795 (1999).
[17]T. Yatsui, M. Kourogi, and M. Ohtsu, Appl. Phys. Lett. **73**, 2090 (1998).
[18]M. N. Islam, X. K. Zhao, A. A. Said, S. S. Mickel, and C. F. Vail, Appl. Phys. Lett. **71**, 2886 (1997).
[19]B. Dragnea, J. Preusser, J. M. Szarko, L. McDonough, S. R. Leone, and W. D. Hinsberg, Appl. Surf. Sci. (in press).
[20]*Infrared Fiber Optics*, edited by J. S. Sanghera and I. D. Aggarwal (Chemical Rubber Corp., Boca Raton, 1998).
[21]M. A. Unger, D. A. Kossakovski, R. Kongovi, J. L. Beauchamp, and J. D. Baldeschwieler, Rev. Sci. Instrum. **69**, 2988 (1998).
[22]D. B. Talley *et al.*, Mater. Lett. **42**, 339 (2000).
[23]A. Larech, R. Bachelot, P. Gleyzes, and A. C. Boccara, Appl. Phys. Lett. **71**, 575 (1997).
[24]B. Knoll and F. Keilmann, Nature (London) **399**, 134 (1999).
[25]K. Fukuzawa and Y. Tanaka, Appl. Phys. Lett. **71**, 169 (1997).
[26]F. Zenhausern, M. P. O'Boyle, and H. K. Wickramasinghe, Appl. Phys. Lett. **65**, 1623 (1994).

[27]D. P. E. Smith, Rev. Sci. Instrum. **66**, 3191 (1995).

[28]B. Hecht, H. Bielefeldt, Y. Inouye, and D. W. Pohl, J. Appl. Phys. **81**, 2492 (1997).

[29]C. J. R. Sheppard, T. J. Connolly, J. Lee, and C. J. Cogswell, Appl. Opt. **33**, 631 (1994).

[30]C. E. Jordan, S. J. Stranik, L. J. Richter, and R. R. Cavanagh, J. Appl. Phys. **86**, 2785 (1999).

[31]J. A. Cline and M. Isaacson, Appl. Opt. **34**, 4869 (1995).

[32]C. J. Bouwkamp, Philips Res. Rep. **5**, 321 (1950).

[33]Y. Leviatan, J. Appl. Phys. **60**, 1577 (1986).

[34]J. A. Cline and M. Isaacson, Ultramicroscopy **57**, 147 (1995).

[35]T. R. Corle and G. S. Kino, *Confocal Scanning Optical Microscopy and Related Imaging Systems* (Academic, New York, 1996), p. 22.

[36]L. H. Sperling, *Introduction to Physical Polymer Science* (Wiley, New York, 1992).

[37]J. J. Greffet and R. Carminatti, Prog. Surf. Sci. **56**, 133 (1997).